1 **Evaporation and sublimation measurement and modelling of an alpine saline lake influenced by**

2 **freeze–thaw on the Qinghai–Tibet Plateau**

3 Fangzhong Shi[1,2,3], Xiaoyan Li[1,2,4,5], Shaojie Zhao[1,2], Yujun Ma[6], Junqi Wei[1,2], Qiwen Liao[1,2], Deliang

4 Chen[7]

5 [1]State Key Laboratory of Earth Surface Processes and Resource Ecology, Faculty of Geographical

6 Science, Beijing Normal University, Beijing 100875, China;

7 [2]School of Natural Resources, Faculty of Geographical Science, Beijing Normal University, Beijing

8 100875, China

9 [3]Research and Development Center for Watershed Environmental Eco−Engineering, Beijing Normal

10 University at Zhuhai, Zhuhai, 519085, China;

11 [4]Key Laboratory of Tibetan Plateau Land Surface Processes and Ecological Conservation, Ministry of

12 Education, Qinghai Normal University, Xining, China

13 [5]Academy of Plateau Science and Sustainability, Qinghai Normal University, Xining, China

14 [6]School of Geography and Planning, Sun Yat–sen University, Guangzhou, China

15 [7]Regional Climate Group, Department of Earth Sciences, University of Gothenburg, Gothenburg,
16 Sweden.

17 * To whom the correspondence should be addressed: Xiao–Yan Li, State Key Laboratory of Earth

18 Surface Processes and Resource Ecology, Beijing Normal University, Beijing, China. Emails:

19 xyli@bnu.edu.cn.

20 ✉ **Fangzhong Shi (during review)**   **fzshi@mail.bnu.edu.cn**

21 ✉ **Xiaoyan Li* (after acceptance)**   **xyli@bnu.edu.cn**

22

23

Key Points

- Night evaporation of Qinghai Lake accounts for more than 40% of the daily evaporation during both the ice–free and ice–covered periods.

- Lake ice sublimation reaches 175.22±45.98 mm, accounting for 23% of the annual evaporation.

- Wind speed weakening may have resulted in an 7.56% decrease in lake evaporation during the ice–covered period from 2003 to 2017.

Abstract

Saline lakes on the Qinghai–Tibet Plateau (QTP) affect the regional climate and water cycle through water loss (E, evaporation under ice–free and sublimation under ice–covered conditions). Due to the observation difficulty over lakes, E and its underlying driving forces are seldom studied targeting saline lakes on the QTP, particularly during the ice–covered periods (ICP). In this study, The E of Qinghai Lake (QHL) and its influencing factors during the ice–free periods (IFP) and ICP were first quantified based on six years of observations. Subsequently, three models were calibrated and compared in simulating E during the IFP and ICP from 2003 to 2017. The annual E sum of QHL is 768.58 ± 28.73 mm, and the E sum during the ICP reaches 175.22 ± 45.98 mm, accounting for 23% of the annual E sum. E is mainly controlled by the wind speed, vapor pressure difference, and air pressure during the IFP, but is driven by the net radiation, the difference between the air and lake surface temperatures, wind speed, and ice coverage during the ICP. The mass transfer model simulates lake E well during the IFP, and the model based on energy achieves a good simulation during the ICP. Moreover, wind speed weakening resulted in an 7.56% decrease in E during the ICP of 2003~2017. Our results highlight the importance of E in ICP, provide new insights into saline lake E in alpine regions, and can be used as a reference to further improve hydrological models of alpine lakes.

Keywords:

Lake evaporation and sublimation, saline lakes, flux observation, ice–covered periods, Qinghai Lake, Qinghai–Tibet Plateau

1. Introduction

Saline lakes account for 23% of the total area and 44% of the total water volume of Earth's lakes (Wurtsbaugh et al., 2017). They are critical in shaping the regional climate and maintaining ecological security and sustainable development in arid regions (Messager et al., 2016; Wurtsbaugh et al., 2017; Woolway et al., 2020; Wu et al., 2021; Wu et al., 2022). Under the influences of climate change and human activities, saline lakes worldwide have changed rapidly in terms of their area, level, temperature, ice phenology, energy, and water exchange, which has become an issue of concern (Gross, 2017; Wurtsbaugh et al., 2017; Woolway et al., 2020). Evaporation under ice–free periods (IFP) and sublimation under ice–covered periods (ICP) are important mechanisms of the transfer of energy and water between lakes and the atmosphere, and are among the major factors influencing changes in lake water volume (Ma et al., 2016; Zhu et al., 2016; Woolway et al., 2018; Guo et al., 2019; Woolway et al., 2020).

In contrast to freshwater lakes, E (evaporation under IFP and sublimation under ICP) of saline lakes involves a more complex process and is affected not only by climate conditions, lake depth, temperature, stratification, thermal stability, and hydrodynamics, but also by salinity (Salhotra et al., 1985; Hamdani et al., 2018; Obianyo, 2019; Woolway et al., 2020). For example, dissolved salt ions can reduce the free energy of water molecules (i.e., reduce water activity) and result in a reduced saturated vapor pressure above saline lakes at a given water temperature (Salhotra et al., 1987; Mor et al., 2018). Previous studies have investigated the relationship between the E and salinity of saline lakes, and discrepancies in the controlling factors between different time scales (Salhotra et al., 1987; Lensky et al., 2018; Hamdani et al., 2018; Mor et al., 2018). These studies have mainly focused on saline lakes in arid and temperate zones, and the interaction and mutual feedback between the water body of saline lakes and the atmosphere remain unclear. There are few studies on the E of alpine saline lakes that exhibit complex hydrology and limnology.

Saline lakes account for over 70% of the total lake area on the Qinghai–Tibet Plateau (QTP) (Liu et al., 2021), and thus profoundly affect the regional climate and water cycle through the E (Yang et al., 2021). However, continuous year–round direct measurements of saline lake E are scarce, which hinders the exploration of lake E at different time scales. Observations of E from saline lakes have been obtained for

4

77   Qinghai Lake (QHL) (Li et al., 2016), Namco (Wang et al., 2015; Ma et al., 2016), Selinco (Guo et al.,

78   2016), and Erhai (Liu et al., 2015) via the eddy–covariance (EC) technique or pan E on the QTP, but

79   these observations are mainly during the IFP (approximately mid–May to mid–October). Thus, there are

80   considerably fewer E observations during the ICP and full–year period of lakes, mostly because of the

81   harsh environment and limited accessibility to the QTP (Zhu et al., 2016). However, most lakes on the

82   QTP exhibit a long and stable ICP lasting more than 100 days due to the low annual air temperature (Ta)

83   (Cai et al., 2019), which suggests that E observations are currently lacking for nearly a quarter of the year

84   (from the IFP to the ICP). Although studies have commented on the importance of E during the ICP (Li

85   et al., 2016; Wang et al., 2020), and clarified that freezing/breakup processes could result in sudden

86   changes in lake surface properties (such as albedo and roughness) and affect the water and energy

87   exchange between the lake and atmosphere (Cai et al., 2019; Yang et al., 2021). the dynamic processes

88   of energy interchange and E of saline lakes during the ICP and its responses to climatic variability on the

89   QTP still constitute a knowledge gap in lake hydrology research. Thus, there is an urgent need to better

90   quantify lake E during the ICP on the QTP.

91   Many models have been employed to calculate lake E, mainly including the Dalton formula series based

92   on mass transfer and aerodynamics, energy and water balance formula series, Penman formula series

93   considering both aerodynamics and energy balance, and empirical formulas based on statistical analysis

94   (Dalton, 1802; Bowen, 1926; Penman, 1948; Harbeck et al., 1958; Finch and Calver, 2008; Hamdani et

95   al., 2018; Wang et al., 2019a). However, the reported values exhibit large discrepancies in their seasonal

96   variations and annual amounts between those models (Zhu et al., 2016; Ma et al., 2016; Guo et al., 2019;

97   Wang et al., 2019a; Wang et al., 2020), and almost all models were calibrated and verified against E

98   observations during the IFP, while E during the ICP was either not calculated or unverified (Wang et al.,

99   2020), as a result of the deficiency in observed E during the ICP (Zhu et al., 2016; Guo et al., 2019). In

100   addition, compared with small lakes, large and deep lakes exhibit higher E levels and delayed seasonal

101   E peaks because more energy is absorbed and stored in large and deep lakes during the IFP and released

102   during the ICP (Wang et al., 2019a). Thus, the effect of changes in ice phenology on lake E is particularly

103   important, which calls for different models for E simulation during the IFP and ICP.

104   Furthermore, with increasing overall surface air warming and moistening, solar dimming, and wind

stilling since the beginning of the 1980s (Yang et al., 2014), lakes on the QTP have experienced a

significant temperature increase (at a rate of 0.037 °C yr^{-1} from 2001 to 2015) (Wan et al., 2018) and ice

phenology shortening (at a rate of −0.73 d yr^{-1} from 2001 to 2017) (Cai et al., 2019). Changes in Ta,

water surface temperature (Ts), wind speed (WS), and ice phenology could impose different effects on

energy interchange and molecular diffusion due to differences in the state phase and reflectance of water

between the ICP and IFP, thus altering lake E (Wang et al., 2018). Although many studies have reported

a decrease in lake E on the QTP by model simulations (Ma et al., 2016; Zhu et al., 2016; Li et al., 2017;

Guo et al., 2019), owing to E neglect during the ICP, the potential mechanisms of lake E and its different

responses to climate variability during the ICP and IFP remain unclear.

In this study, based on six continuous years of direct measurements of lake E and energy exchange flux

data obtained with the EC technique pertaining to QHL, the largest saline lake on the QTP, between 2014

and 2019, we quantified the characteristics of energy interchange and E on diurnal, seasonal (IFP, ICP

and cycle year: AN) and yearly time scales and identified the potential factors influencing E during the

IFP and ICP. In addition, combined with reanalysis climate datasets, a mass transfer model (MT model),

an atmospheric dynamics model (AD model), and a model based on energy, temperature and WS (JH

model) were calibrated and verified, with the optimal model chosen for the simulation of lake E and its

response to climatic variability during the IFP and ICP from 2003 to 2017. The results highlight the

importance and potential mechanisms of E during ICP, and can be used as a reference to further improve

hydrological models of alpine lakes.

2. Materials and Methods

2.1. Study area

QHL (36°32′~37°15′ N, 99°36′~100°47′ E, 3194 m a.s.l.), with an area of 4,432 km^2 and a catchment of

29,661 km^2, is the largest inland saline lake in China (Li et al., 2016). The average depth of the lake is

26 m. The average salt content is 14.13 g L^{-1}, and the pH ranges from 9.15 to 9.30. The hydrochemical

type of the lake water is Na–SO$_4$–Cl (Li et al., 2016). Surrounded by mountains, the QHL is a typical

closed tectonic depression lake, which is fed by five major rivers, including the Buha, Shaliu, Hargai,

Quanji, and Heima Rivers (Jin et al., 2015). The total annual water discharge is approximately 1.56×10^9

132   m^3, of which the Buha River contributes 50% and Shaliu River contributes approximately one third (Jin

133   et al., 2015). The mean annual Ta, precipitation, and E values between 1960 and 2015 were −0.1 °C, 355

134   mm and 925 mm, respectively (Li et al., 2016). The seasonal stratification of QHL corresponded to that

135   of a dimictic lake with the spring overturn taking place around May and the autumn overturn appearing

136   around November–December (Su et al., 2019). The ICP usually begins in late November, ends in mid–

137   late March or even early April, and lasts approximate 100 days. Under the effects of climate warming,

138   QHL has experienced temperature increases, area expansion, and ICP shortening in the last two decades

139   (Tang et al., 2018; Han et al., 2021).

2.2. Site description and energy exchange flux and climate data

141   The instruments to measure the energy exchange flux and micrometeorological parameters were installed

142   at the China Torpedo Qinghai Lake test base (36°35′27.65″ N, 100°30′06″ E, 3198 m a.s.l.) located in

143   the southeastern QHL approximately 737 m from the nearest shore (Li et al., 2016) (Fig. 1). The water

144   depth underneath this platform is 18 m. The torpedo test tower has a height of 10 m above the water

145   surface. The EC system was installed on a steel pillar mounted on the northwestern side of the top of the

146   torpedo test tower with a total height of 17.3 m above the lake water surface (Li et al., 2016). A three–

147   dimensional sonic anemometer (model CSAT3, Campbell Scientific Inc., Logan, UT, USA) was used to

148   directly measure horizontal and vertical wind velocity components (u, v, and w) and virtual temperature.

149   An open–path infrared gas analyzer (model EC150, Campbell Scientific Inc.) was applied to measure

150   fluctuations in water vapor and carbon dioxide concentrations. Fluxes of sensible heat (H) and latent heat

151   (LE) were calculated from the 10–Hz time series at 30–min intervals and recorded by a data logger

152   (CR3000, Campbell Scientific Inc.). The observation instruments were powered by solar energy.

153   A suite of auxiliary micrometeorology was also measured as 30–min averages of 1–s readings on the

154   eastern side of the top of the torpedo test tower, 3 m from the EC instruments. The net radiation (Rn) was

155   calculated from the incoming shortwave, reflected shortwave, and incoming and outgoing longwave

156   radiation, which were measured by a net radiometer (CNR4, Kipp & Zonen B.V., Delft, Netherlands) at

157   10 m above the lake surface (Fig. 1; Table S1). The Ta, relative humidity (RH), and air pressure (Pres)

158   were measured at a height of 12.5 m above the water surface (Table S1). A wind sentry unit (model 05103,

159   RM Young, Inc. Traverse City, MI, USA) was employed to measure the WS and wind direction (WD)

160   (Table S1). The Ts was measured with an infrared thermometer (model SI–111, Campbell Scientific Inc.)

161   approximately 10 m above the water surface, and the water temperature (Tl) was measured with five

162   temperature probes (109 L, Campbell Scientific Inc.) at depths of 0.2, 0.5, 1.0, 2.0, and 3.0 m.

163   Precipitation was measured with an automated tipping–bucket rain gauge (model TE525, Campbell

164   Scientific Inc.) and precipitation gauge (model T–200B, Campbell Scientific Inc.) (Table S1). The

165   observation system began operation on May 11, 2013. In this study, we unified all observational data at

166   30–min intervals and analyzed the data from January 1, 2014 to December 31, 2019 (Table S1).

167   **2.3. Reanalysis climate datasets**

168   The reanalysis climate datasets used to drive the lake E models were acquired from the interim reanalysis

169   dataset v5 (ERA5) produced by the European Centre for Medium–Range Weather Forecasts

170   (https://cds.climate.copernicus.eu/cdsapp#!/search?type=dataset) and the China Regional High–

171   Temporal–Resolution Surface Meteorological Elements–Driven Dataset (CMFD)

172   (http://data.tpdc.ac.cn/en/). Gridded hourly ERA5 skin temperature and daily WS, daily CMFD Ta, Pres,

173   RH, and downward shortwave radiation (Rs) at a spatial resolution of 0.1° from 2001 to 2018 were

174   analyzed in this study (Table S1). The daily skin temperature was generated by averaging the hourly

175   temperature over 24 h per day and was adopted as the lake surface temperature. We extracted climate

176   data pertaining to QHL via a grid mask with a spatial resolution of 0.1° and averaged the data in all pixels.

177   Considering the advantages of long–time spans and high resolution, the ERA5 and CMFD datasets

178   developed based on land station data have been recognized as the best currently available reanalysis

179   products and have been widely applied in land–surface and hydrological modeling studies in China (Ma

180   et al., 2016; Zhu et al., 2016; Tian et al., 2021; Xiao and Cui, 2021). To reduce the uncertainty caused by

181   the input data, the daily lake surface temperature and WS from EAR5, Ta, Rs, RH, and Pres from CMFD

182   for QHL were adjusted with fitting equations of the observed daily Ts ($R^2 = 0.92$, $P < 0.01$), WS ($R^2 =$

183   0.55, $P < 0.01$), Ta ($R^2 = 0.90$, $P < 0.01$), Rs ($R^2 = 0.73$, $P < 0.01$), RH ($R^2 = 0.63$, $P < 0.01$), and Pres (R^2

184     $= 0.95$, $P < 0.01$) from 2014 to 2018 (Fig. S1), and the equations are shown below:

185 $$Ta^{ad} = 1.01 \times Ta^{CMFD} + 0.71 \tag{1}$$

186 $$Ts^{ad} = 0.71 \times Ts^{ERA5} + 3.30 \tag{2}$$

$$\text{Rs}^{ad} = 0.86 \times \text{Rs}^{CMFD} + 34.63 \qquad (3)$$

$$WS^{ad} = 0.60 \times \text{WS}^{ERA5} + 0.76 \qquad (4)$$

$$\text{RH}^{ad} = 0.68 \times \text{RH}^{CMFD} + 19.95 \qquad (5)$$

$$\text{Pres}^{ad} = 0.97 \times \text{Pres}^{CMFD} + 30.72 \qquad (6)$$

Where Ta^{ad}, Ts^{ad}, Rs^{ad}, WS^{ad}, RH^{ad}, and Pres^{ad} are Ta, Ts Rs, WS, RH, and Pres of ERA5 and CMFD after adjustment, respectively.

2.4. Lake ice coverage dataset and ice phenology

The daily lake ice coverage of QHL from 2002 to 2018 was extracted from a lake ice coverage dataset of 308 lakes (with an area greater than 3 km^2) on the QTP retrieved from the National Tibetan Plateau Data Center (https://doi.org/10.11922/sciencedb.744). The dataset with a time span from 2002 to 2018 was generated from the Moderate Resolution Imaging Spectroradiometer (MODIS) normalized difference snow index (NDSI, with a spatial resolution of 500 m) product with the SNOWMAP algorithm, and the data under cloud cover conditions were redetermined based on the temporal and spatial continuity of lake surface conditions (Qiu et al., 2019). Based on the lake ice coverage, the IFP was defined as ice coverage lower than 10%, and the ICP was defined as ice coverage higher than 10% (Qiu et al., 2019). The ICP was divided into three stages: freeze (FZ: 10% < ice coverage < 90%), completely freeze (CF: ice coverage > 90%) and thaw (TW: 10% < ice coverage < 90%) (Qiu et al., 2019). We defined the cycle year (annual: AN) from the beginning of the IFP to the end of the ICP. This ice coverage has been compared with that from two other datasets based on passive microwave, and was found to be highly consistent with each other at an average R^2 of 0.86 and an RMSE of 0.13 in QHL (Qiu et al., 2019). Thus, this dataset is very accurate and suitable for the division of lake ice phenology in QHL.

2.5 Data processing of the observed energy exchange flux and climate data

The EC fluxes were processed and corrected based on the 10–Hz raw time series data in the data processing software EdiRe, including spike removal, lag correction of water to carbon dioxide relative to the vertical wind component, sonic virtual temperature correction, performance of planar fit coordinate rotation, density fluctuation correction (WPL correction) and frequency response correction (Li et al.,

213   2016). Since the shortest distance between the Chinese torpedo Qinghai Lake test base and the

214   southwestern lakeshore is only 737 m, there may be insufficient fetch for a turbulent flux under certain

215   conditions. Therefore, footprint analysis was conducted to eliminate data influenced by the surrounding

216   land. For further details on the process and results of the footprint analysis, see Li et al. (2016). In addition

217   to these processing steps, quality control of the 30–min flux data was conducted using a five–step

218   procedure: (i) data originating from periods of sensor malfunction were rejected (e.g., when there was a

219   faulty diagnostic signal), (ii) data within 1 h before or after precipitation were rejected, (iii) incomplete

220   30–min data were rejected when the missing data constituted more than 3% of the 30–min raw record,

221   (iv) data were rejected at night when the friction velocity was below 0.1 m s^{-1} (Blanken et al., 1998) and

222   (v) data with large footprints (>700 m) and a wind direction from 180° to 245° were eliminated.

223   To further control the quality of the energy exchange flux (sensible heat flux and latent heat flux: H and

224   LE, respectively) and micrometeorological dataset (Rn, Ta, Ts, Tl, RH, WS, Pres, and albedo), data

225   outside the mean ± 3 × standard deviation were removed for each variable. Then, gap–filling methods

226   entailing a look–up table and mean diurnal variation (Falge et al., 2001) were adopted to fill gaps in the

227   flux measurement data. The look–up table method was applied when the meteorological dataset was

228   available synchronously. Otherwise, the mean diurnal variation method was adopted. The heat storage

229   change (G, W m^{-2}) was estimated as a residual of the energy balance:

$$G = Rn - LE - H \qquad (7)$$

231   where Rn is the net radiation (W m^{-2}), H is the sensible heat flux (W m^{-2}) and LE is the latent heat flux

232   (W m^{-2}). Lake E was calculated as

$$E = \lambda \times LE \qquad (8)$$

234   where λ is the latent heat of vaporization (MJ kg^{-1}), taken as 2.45 MJ kg^{-1} in this paper (Allen et al.,

235   1998).

236   **2.6. Models for daily lake evaporation simulation**

237   To evaluate the interannual variation in QHL E from 2003 to 2017, we validated three models during the

238   AN, IFP, and ICP. Considering that Qinghai Lake is a saline lake, and many studies have pointed out that

239   it is valuable to consider the influence of salinity on saline lake evaporation, and with the increase of

240 salinity, it will exert greater inhibition on evaporation (Hamdani et al., 2018; Mor et al., 2018). Thus, the

241 water activity coefficient (α) which is defined as the ratio between the vapor pressure above saline water

242 and that above freshwater at the same temperature has been introduced to characterize the effect of

243 salinity on saline lake evaporation (Salhotra et al., 1987; Lensky et al., 2018). Because saline water drains

244 out salt during freezing (Badawy, 2016), we only introduced the α into the evaporation simulation of

245 Qinghai Lake during IFP. The three models were as follows:

246 1) Mass–transfer model (MT model) (Harbeck et al., 1958)

247
$$E_{MT} = N \times F(WS) \times \Delta e \tag{9}$$

248
$$F(WS) = a1 \times WS + a2 \tag{10}$$

249
$$\Delta e = \begin{cases} \alpha \times e_s - RH \times e_a & \text{During IFP} \\ e_s - RH \times e_a & \text{During ICP} \end{cases} \tag{11}$$

250
$$e_s = 6.105 \times \exp\left(\frac{17.27 \times Ts}{Ts + 237.7}\right) \tag{12}$$

251
$$e_a = 6.105 \times \exp\left(\frac{17.27 \times Ta}{Ta + 237.7}\right) \tag{13}$$

252 where E_{MT} is the E rate (mm d^{-1}); N is the mass–transfer coefficient; WS is the wind speed (m s^{-1}); Δe

253 is the vapor pressure difference, e_s and e_a are the saturated vapor pressures at the lake surface

254 temperature (Ts) and air temperature (Ta), respectively. And an α value of 0.97 was suggested for QHL

255 during IFP, as measured with a portable water activity meter (AwTester, China). This model inherently

256 accounts for the water salinity through Δe and requires calibration of coefficients N, a1, and a2, which

257 were taken as 1.26, 0.04, and 0.17, respectively, during the AN; 0.41, 0.17, and 0.28, respectively, during

258 the IFP; and 0.90, 0.18, and 0.28, respectively, during the ICP in this study.

259 2) Atmospheric dynamics model (AD model) (Hamdani et al., 2018)

260
$$E_{AD} = \frac{0.622 \times Ce}{\rho_w \times P} \times \rho_a \times WS \times 3.6 \times 10^6 \times \Delta e \tag{14}$$

261
$$\rho_a = 1.293 \times \left(\frac{273.15}{273.15 + Ta}\right) \times \frac{Pres}{101.325} \tag{15}$$

262 where ρ_w and ρ_a denote the water and air densities (kg m^{-3}), respectively, and ρ_w is approximately

263 1.011 $\times$ 10^3 kg m^{-3} for QHL. Moreover, $Pres$ is the air pressure (mbar), and Ce is a transport

264   coefficient obtained via calibration to address missing friction velocity values in the reanalysis climate

265   datasets, which was taken as 4.10×10^{-3}, 3.80×10^{-3}, and 8.40×10^{-3} during the AN, IFP, and ICP,

266   respectively, in this paper.

267   3) Statistical model based on solar radiation (the Jensen–Haise method: JH model) (Wang et al., 2019a)

268    $$E_{JH} = JH1 \times (JH2 \times (Ta - Ts) + JH3) \times (Rs) \times (WS) \qquad (16)$$

269   where Rs is the incoming solar shortwave radiation (W m^{-2}); JH1, JH2, and JH3 must be calibrated

270   and were taken as 0.06, -2.20×10^{-3}, and 5.03×10^{-3}, respectively, during the AN; 0.08, -2.00×10^{-3},

271   and 0.04, respectively, during the IFP; and 0.02, 7.40×10^{-3}, and 0.18, respectively, during the ICP in

272   this paper.

273   The three models were selected, first, as they are typical representatives in considering mass transfer,

274   aerodynamics, and energy transfer; second, because their demand parameters are easy to acquire, which

275   are adaptive to be promoted; and third, as they have been proven to be efficient in saline lakes (Hamdani

276   et al., 2018). These models were first calibrated and validated based on daily E observations from 2014

277   to 2019 during AN, IFP, and ICP, respectively. The root–mean–square error (RMSE) and goodness of fit

278   (R^2) were used to evaluate the effectiveness of the models. A model with high R^2 and low RMSE values

279   was selected for lake E simulation during the AN, IFP, and ICP.

280   **2.7. Statistical analysis**

281   Summer and autumn were taken as June to August and September to November, respectively. During

282   data analysis, we first divided the 30–min observed energy exchange flux and climate data from 2014 to

283   2019 by the AN, IFP, and ICP based on the calculated ice phenology. Hence, we obtained datasets of five

284   cycle years from the IFP in 2014 to the ICP in 2018 (Fig. S2). Second, we calculated the multiday average

285   30–min energy exchange flux during the IFP and ICP in each year to evaluate the basic statistical

286   characteristics of the diurnal E and exchange flux. The daily energy exchange flux and climate data were

287   calculated by averaging the 30–min observed data for each day, the daytime (nighttime) energy exchange

288   flux and climate data were calculated by averaging the 30–min observed data of 8:00 am to 7:30 pm

289   (8:00 pm to 7:30 am). And one–way ANOVA was performed to compare the difference in E and G

290   between the IFP and ICP in each year from 2014 to 2018. Third, to explore the key factor controlling

291 lake E, partial least squares regression and random forest methods were used to calculate the sensitivity

292 coefficient (representing the regression coefficient of each variable, which means the amount of change

293 in E caused by the variation of per unit in the variable) and importance of Rn, WS, Δe, Pres, albedo, WD,

294 Ta−Ts, Tl, and ICR to E during the daytime and nighttime of IFP and ICP, respectively. The two methods

295 analyze the relationship between E and climate and environmental factors from linear and nonlinear

296 processes, respectively, and have been widely used in the study of hydrological and ecological fields

297 (Desai and Ouarda, 2021; Li et al., 2022; Sow et al., 2022). Finally, three models were validated and two

298 models were selected to severally calculate the interannual E during the IFP and ICP from 2003 to 2017

299 (the available ice phenology exhibits a limited cycle year from 2003 to 2017). Four controlled tests were

300 then conducted to quantify the contribution of the variation in Ta, Ts, WS, and Rs to lake E from 2003 to

301 2017. The analysis of partial least squares regression, random forest methods, and E simulation,

302 calibration and verification were conducted by daily datasets. The partial least squares and random forest

303 analyses were conducted in R and the others were conducted in MATLAB.

304 **3. Results**

305 **3.1. Diurnal and seasonal characteristics of evaporation and the energy budget during the different**

306 **freeze–thaw periods**

307 The average E, LE, G, H, and Rn values (average from 2014 to 2018) were 1.20 ± 0.09 mm d^{-1}, $68.01 \pm$

308 4.93 W m^{-2}, 192.18 ± 7.00 W m^{-2}, 16.25 ± 1.21 W m^{-2}, and 276.45 ± 3.32 W m^{-2}, respectively, during

309 the IFP; and 1.11 ± 0.20 mm d^{-1}, 63.15 ± 11.31 W m^{-2}, 79.23 ± 18.12 W m^{-2}, 4.68 ± 0.37 W m^{-2}, and

310 147.06 ± 14.23 W m^{-2}, respectively, during the ICP. The daytime E, LE, G, H, and Rn values were notably

311 lower during the ICP than during the IFP, except for E and LE in 2014 (Figs. 2 and 3; Table S2). In

312 addition, the daily peak LE and E values typically occurred at approximately 12 pm during the IFP and

313 approximately 2 pm during the ICP, and exhibited an approximately two–hour lag during the IFP and a

314 four–hour lag during the ICP over G and Rn (Fig. 2). At night, although lower E (at an average rate of

315 0.81 ± 0.17 mm d^{-1}) and LE (46.02 ± 9.71 W m^{-2}) levels occurred during the ICP than during the IFP (at

316 average rates of 0.94 ± 0.05 mm d^{-1} and 53.09 ± 2.94 W m^{-2}, respectively), E (LE) accounted for 42%~45%

317 and 41%~45% of the total daily E during the IFP and ICP, respectively (Figs. 2 and 3; Table S2).

13

318 Regarding G, a similar release rate was found during IFP and ICP, but the heat release time was longer

319 during ICP than during IFP (Fig. 2).

320 The daily E ranged from 1.96 to 2.34 mm d^{-1} during the IFP and from 1.57 to 2.71 mm d^{-1} during the

321 ICP, and the average E sum reached 593.37 ± 44.87 mm yr^{-1} during the IFP and 175.22 ± 45.98 mm yr^{-}

322 ^{1} during the ICP from 2014 to 2018 (Figs. 3 and S2; Table S2). This suggested an average E sum of 77%

323 during the IFP and 23% during the ICP throughout the cycle year from 2014 to 2018 (with a lake E sum

324 ranging from 719.45 to 798.55 mm yr^{-1} and an average value of 768.58 ± 28.73 mm yr^{-1}) (Fig. 3). In

325 terms of G, QHL initially released heat in autumn, which lasted until the lake was completely frozen,

326 after which heat was absorbed from the lake thawing period throughout the summer (Figs. S2 and S3).

3.2. Response of evaporation to climatic factors during the different freeze–thaw periods

328 The key controlling factor of lake E was explored based on the daily observed energy exchange flux and

329 climate data (E, Rn, WS, Δe, Pres, albedo, WD, Ta−Ts, and Tl) and ICR during the IFP and ICP from

330 2014 to 2018. The Δe (with a sensitivity coefficient of 0.28 in the daytime and 0.22 in the nighttime, P <

331 0.05), WS (with a sensitivity coefficient of 0.54 in the daytime and 0.43 in the nighttime, P < 0.05) and

332 Pres (with a sensitivity coefficient of 0.26 in the daytime and 0.14 in the nighttime, P < 0.05) notably

333 increased E (Fig. 4), and the effect was greater in the daytime than in the nighttime during the IFP (Fig.

334 4). The Rn (with a sensitivity coefficient of 0.25 in the nighttime, P < 0.05), WS (with a sensitivity

335 coefficient of 0.30 in the daytime and 0.22 in the nighttime, P < 0.05), Ta−Ts (with a sensitivity coefficient

336 of 0.59 in the daytime and 0.39 in the nighttime, P < 0.05) and ICR (with a sensitivity coefficient of 0.20

337 in the daytime and 0.17 in the nighttime, P < 0.05) imposed a significant positive effect on E during the

338 ICP (Fig. 4). Similarly, the top five important factors calculated with the random forest method were WS,

339 Δe, Pres, WD, and Ts during the IFP and Ta−Ts, Ta, WS, Rn, and ICR during the ICP (Fig. S4). This

340 indicated that E of QHL was mainly controlled by WS, Δe, and Pres during the IFP but was driven by

341 Rn, Ta−Ts, WS, and ICR during the ICP.

3.3. Evaporation simulation and interannual variation

343 Three models (MT, AD, and JH) were calibrated and validated to evaluate the interannual variation in

344 QHL E from 2003 to 2017. In the case of model performance, the MT model based on molecular diffusion

345   performed the best in terms of E simulation during the IFP (with the largest R^2 and smallest RMSE values

346   of 0.79 and 0.85, respectively), while the JH model based on energy exchange performed the best during

347   the ICP (with the largest R^2 and smallest RMSE values of 0.65 and 1.02, respectively) (Figs. S5 and S6).

348   Thus, the interannual variation in QHL E from 2003 to 2017 was calculated with the MT model during

349   the IFP and with the JH model during the ICP (Fig. 5). From 2003 to 2017, increases in Δe (at a rate of

350   0.01 hPa yr^{-1}) and Ts (at a rate of 0.001 °C yr^{-1}) resulted in an increase in E (at a rate of 1.62 mm yr^{-1} for

351   the E sum) during the IFP (Figs. 5 and S7). Conversely, ignoring the increases in Ta (at a rate of 0.04 °C

352   yr^{-1}) and Ta−Ts (at a rate of 0.04 °C yr^{-1}), with decreasing WS (at a rate of −0.005 m s^{-1} yr^{-1}), E (at a rate

353   of −1.98 mm yr^{-1} for the E sum) decreased during the ICP, which resulted in an inapparent decrease in E

354   (at a rate of −0.36 mm yr^{-1} for the E sum) during the AN (Figs. 5 and S7).

355   **4. Discussion**

356   **4.1. Lake evaporation during the ice–covered period**

357   The results of this study highlight the important contribution of lake ice sublimation to the total amount

358   of lake E. Due to the low snow coverage of Qinghai Lake in winter (with a maximal snow coverage less

359   than 16% of the area of Qinghai Lake), evaporation and sublimation of lake ice and water are the major

360   sources of E during the ICP of 2013~2018 (Fig S8). The experimental and simulation results of Jambon–

361   Puillet et al. (2018) verified that the E rates of liquid droplets and ice crystals remain the same under

362   unchanged environmental conditions. In this study, the E rate of QHL during the ICP ranged from 1.57

363   to 2.71 mm d^{-1}, approximately 0.73~1.38 times that of liquid water during the IFP (Table S2), with similar

364   results to those findings of liquid droplets and ice crystals. Few studies have examined lake ice E during

365   the ICP, and most of which have focused on polar sea ice and alpine snow packs (Froyland et al., 2010;

366   Froyland, 2013; Herrero et al., 2016; Christner et al., 2017; Lin et al., 2020). Observational and modelling

367   studies of Antarctic ice sheets or lakes have found that the monthly E rate of ice ranged from −4.6 to 13

368   mm $month^{-1}$ from June to September (Antarctic) (Froyland et al., 2010). In this study, we found that the

369   E sum ranges from 130.59 to 262.45 mm during the ICP (approximately 51.60 to 81.3 mm $month^{-1}$, by

370   multiplying the mean daily E of ICP by 30) from 2014 to 2018, which is higher than the previous

371   observations from Antarctic ice sheets or lakes. This may be because Antarctic ice sheets or lakes are

372   located at high latitudes with low solar radiation and are therefore cooler from the surface to greater

373   depths with energy–limiting conditions for E (Persson et al., 2002). However, the lakes on the QTP freeze

374   seasonally, most of these lakes can store a large amount of heat because of the high solar radiation during

375   the IFP (Fig. 6), which lead to the observed E during the ICP (Huang et al., 2011 and 2016). Studies on

376   surface E of a shallow thermokarst lake in the central QTP region have found that E reaches up to 250

377   mm yr^{-1} during the ICP (Huang et al., 2016), which is close to our observed E levels (130.59~262.45

378   mm yr^{-1}). Our results further showed that E of QHL accounted for 23% of the annual E during the ICP.

379   Wang et al. (2020) evaluated 75 large lakes on the QTP and demonstrated that the E of these lakes in

380   winter accounted for 12.3~23.5% of the annual E, which suggests that E of these lakes during the ICP

381   was the same as that during the other seasons. Furthermore, considering that the area of QHL is 4,432

382   km^2 (Li et al., 2016), QHL releases 3.39 ± 0.13 km^3 of water into the air every year, which corresponds

383   to the sum of the water for animal husbandry, industrial and domestic uses in Qinghai Province (an

384   average of 2014 to 2017) (Dong et al., 2021).

385   **4.2. Responses of lake evaporation to salinity**

386   Salinity greatly influences the E of saline lakes by changing both water density and thermal properties,

387   dissolved salt ions can reduce the free energy of water molecules, and result in a higher boiling point and

388   reduced saturated vapor pressure above saline lakes (Salhotra et al., 1987; Abdelrady, 2013; Mor et al.,

389   2018). Therefore, an increase in the salinity of a lake would decrease its E rate. For example, Lee (1927)

390   compared the E of pure water with that of saline lakes of different densities (salinity) in Nevada, USA,

391   and found that when the density (salinity) of water increased by 1%, the E of saline lakes decreased by

392   0.01% compared with that of pure water. Similarly, Mor et al. (2018) found that the E rate in diluted

393   plume is nearly three times larger than that in open lake in the Dead Sea. Thus, the thermodynamic

394   concept of water activity which is defined as the ratio of water vapor pressure on the surface of saline

395   and fresh water at the same temperature (the water activity of freshwater is 1, while that of saline water

396   is lower than 1, and the higher the salinity is, the lower the water activity in lakes) has been widely used

397   in E simulations of saline lakes (Salhotra et al., 1987; Abdelrady, 2013; Mor et al., 2018). In our study,

398   we measured the water activity of QHL as 0.97 by a salinity of 14.13 g L^{-1}, and applied it to the MT and

399   AD models for E simulation of IFP during 2003 to 2017, which make it more theoretical to explain the

400   E process of saline lakes and reduced the uncertainty of estimation in saline lake E. For example, with

401 the salinity of 133 g L^{-1} of surface water, water activity was measured to be 0.65, and has been widely

402 used in its E simulation of the Dead Sea (Metzger et al., 2018; Mor et al., 2018; Lensky et al., 2018); and

403 Abdelrady (2013) improved the surface energy balance system (SEBS) of E in saline lakes by

404 constructing an exponential function between lake salinity and water activity, which reduced the

405 simulated E by 27% and RMSE from 0.62 to 0.24 mm (3h)$^{-1}$ in Great Salt Lake. Therefore, considering

406 salinity is essential to enhance the accuracy of E simulations in saline lakes.

407 **4.3. Responses of lake evaporation to climate variability**

408 In addition, climate and environment are also important factors affecting lake E and vary significantly

409 between the different seasons. Previous studies have shown that lake E is mostly affected by WS and Δe

410 in summer and WS, Δe, Ta−Ts, and G in winter (Zhang and Liu, 2014; Hamdani, et al., 2018). This

411 suggests that energy exchange between lakes and air may be one of the main drivers of E during the ICP

412 under the same atmospheric boundary conditions (Fig. 6). Since most lakes store heat in summer, they

413 release heat and sufficiently produce E in winter (Blanken et al., 2011; Hamdani, et al., 2018). In this

414 study, we also found that QHL began to store heat in the lake thawing period and released heat in autumn

415 or when the lake began to freeze (Figs. 6 and S3). Therefore, E of QHL was mostly controlled by WS,

416 Δe, and Pres during the IFP, whereas it was mainly affected by Rn, Ta−Ts, and WS during the ICP (Fig.

417 6).

418 Furthermore, the QTP has been suffering surface air warming and moistening, solar dimming, and wind

419 stilling since the beginning of the 1980s across the QTP (Yang et al., 2014; Kuang and Jiao, 2016), which

420 affects the hydrothermal processes of the lake, such as increasing Ts and shortening lake ice phenology

421 (Wan et al., 2018; Cai et al., 2019). An increase in Ts enhances the diffusion of water molecules and

422 enlarges Δe between the water surface and the air, which in turn promotes evaporation (Wang et al., 2018;

423 Woolway et al., 2020), while a reduction in solar radiation decreases the energy input of the lake, and

424 wind stilling enhances the stability of the atmosphere above the water surface, which in turn inhibits

425 evaporation (Roderick and Farquhar, 2022; Guo et al., 2019). We found a decrease in E during the AN

426 from 2003 to 2017, due to the steeper decrease in E caused by solar dimming and wind stilling during

427 the ICP than the increase engendered by the increase in Ts during the IFP. From 2003 to 2017, E decreased

428 at an average rate of −6.48 ± 4.77 mm yr^{-1} (3.23%) and −11.17 ± 14.29 mm yr^{-1} (7.56%) due to decrease

429   in Rs and WS during the ICP, respectively (Fig. 7; Table S3), while the increase in Ts increased E at an

430   average rate of 13.58 ± 20.75 mm yr^{-1} (3.54%) during the IFP (Fig. 7; Table S3). Previous studies have

431   found similar results in Selin Co and Namu Co (Zhu et al., 2016; Guo et al., 2019). For example, Guo et

432   al. (2019) found that E was mainly controlled by WS, and a decrease in WS led to a decrease in E from

433   1985 to 2016 in Selin Co.

434   In addition, changes in lake ice phenology significantly affected lake E during the IFP and ICP. Compared

435   with 2003 to 2007 (101.40 ± 7.00 d), the average ICP decreased by 10.8 d from 2013 to 2017 (90.60 ±

436   6.08 d) (Table S3). A shortened ICP suggests a much lower albedo in the cycle year and could result in

437   higher Rs absorption and a shorter period for heat–induced recession, which could increase lake E (Wang

438   et al., 2018). Furthermore, lake E is also affected by the lake area, water level, and physical and chemical

439   properties (Woolway et al., 2020), especially for saline lakes (Salhotra et al., 1987; Mohammed and

440   Tarboton, 2012; Mor et al., 2018). Increasing the water salinity could reduce E (Salhotra et al., 1987;

441   Mor et al., 2018) because the dissolved salt ions could reduce the free energy of water molecules (i.e.,

442   reduced water activity) and result in a lower saturated vapor pressure above saline lakes at a given water

443   temperature (Salhotra et al., 1987; Mor et al., 2018). However, the changes in lake physical and chemical

444   properties attributed to lake freezing increase the complexity of the underlying mechanism, simulation

445   of ice E and its response to climate change, and more studies are needed to further explore interactions

446   between the different factors.

447   **4.4. Limitation**

448   Based on six continuous year–round direct measurements of lake E and energy exchange flux, we

449   determined the E loss during the ICP and calibrated and verified different models for E simulation during

450   the IFP and ICP. Due to the lack of accurate measurements of deep lake temperatures, energy budget

451   closure ratios of EC observations in QHL are not given in this study. EC measurements have been widely

452   used to quantify the E of several global lakes, including Lake Superior in America, Great Slave Lake in

453   Canada, Lake Geneva in Switzerland, Lake Valkea−Kotinen in Finland, and Taihu Lake, Erhai Lake,

454   Poyang Lake, Nam Co, Selin Co and Ngoring Lake in China (Blanken et al., 2000; Vercauteren et al.,

455   2009; Blanken et al., 2011; Nordbo et al., 2011; Wang et al., 2014; Li et al., 2015; Liu et al., 2015; Guo

456   et al., 2016; Li et al., 2016; Ma et al., 2016; Lensky et al., 2018). With most of the known energy budget

457 closure ratios over 0.7, EC observations of lakes are regarded as an accurate and reliable direct

458 measurement method of E, even in lakes over the QTP (Wang et al., 2020). Moreover, compared with

459 land stations, the energy budget closure ratios over lake surfaces can be significantly influenced by the

460 large amount of heat storage (release) during different seasons (Wang et al., 2020), which would increase

461 the uncertainty about the quantification of E. In addition, quantification of E during the ICP depends on

462 accurate ice phenology identification, and a longer ICP suggests more E. Therefore, the different data

463 sources and phenological classification methods of ice phenology comprise one source of uncertainty.

464 Moreover, lake salinity changes dynamically at diurnal, seasonal and interannual scales, but due to the

465 difficulty of continuously observing lake salinity, the fixed water activity in our study may cause the

466 underestimation in E of QHL due to the decrease in salinity by the expansion of QHL. Furthermore, in

467 addition to the traditional lake evaporation models (Dalton formula series, energy and water balance

468 formula series, Penman formula series, and empirical formula based on statistical analysis), the 1D lake

469 thermodynamics model has been widely used for the simulation of lake ice thickness and energy balance

470 (ice sublimation) in ICP (Pour et al., 2017; Stepanenko et al., Xie et al., 2023). Considering that this study

471 was concentrated on verifying the consistency of the accuracy of the traditional models for the

472 evaporation simulation during IFP and ICP. Thus, this study ignored the 1D lake thermodynamics model

473 for ice sublimation. It is suggested to build the observation system of lake thermodynamics parameters,

474 verify and develop a suitable 1D or even 3D lake thermodynamics evaporation models for QHL in future

475 study.

476 **5. Conclusions**

477 In summary, based on six continuous year–round 30–min direct flux measurements throughout the cycle

478 year from 2014 to 2018, the night E of QHL occupied over 40% during both the IFP and ICP. With a

479 multiyear average of 175.22 ± 45.98 mm yr^{-1}, E during the ICP accounted for 23% of the total cycle year

480 E sum, which is an important component in calculating the E of saline lakes. A difference–based control

481 factor of E was also found during the IFP and ICP. E of QHL was mainly controlled by atmospheric

482 dynamic factors (WS, Δe, and P) during the IFP, whereas it was driven by both energy exchange and

483 atmospheric boundary conditions (Rn, Ta−Ts, and WS) during the ICP. Thus, the MT model based on

484 molecular diffusion performed best in lake E simulation during the IFP, while the JH model based on

energy exchange performed best during the ICP. Furthermore, simulation of the E of QHL showed a slight decrease from 2003 to 2017, caused by a decrease in E during the ICP, and WS weakening may have resulted in an average reduction of 7.56% in lake E during the ICP from 2003 to 2017. Our results suggest that E during the ICP is non–negligible for saline lake E, and E simulation should be further improved in future model simulation studies, considering the difference in its potential mechanisms during the ICP.

Author Contributions

XY Li conceived the idea, and FZ Shi performed the analyses. XY Li, FZ Shi, DL Chen, and YJ Ma led the manuscript writing. SJ Zhao, YJ Ma, JQ Wei, and QW Liao provided analysis of datasets. All authors contributed to the review and the revision of the manuscript.

Acknowledgements

Competing interests

The contact author has declared that the authors have no any competing interests

511

References

513 Abdelrady, A. R. Evaporation over fresh and saline water using SEBS. 2013. Master's Thesis. University
514 of Twente.

515 Allen, R. G., Pereira, L. S., Raes, D., & Smith, M. 1998. Crop evapotranspiration–Guidelines for
516 computing crop water requirements–FAO Irrigation and drainage paper 56. Fao, Rome, 300(9), D05109.

517 Badawy, S. M. 2016. Laboratory freezing desalination of seawater. Desalination and Water Treatment,
518 57(24), 11040-11047.

519 Blanken, P. D., Black, T. A., Neumann, H. H., Den Hartog, G., Yang, P. C., Nesic, Z., ... & Novak, M. D.
520 1998. Turbulent flux measurements above and below the overstory of a boreal aspen forest. Boundary–
521 Layer Meteorology, 89(1), 109–140.

522 Blanken, P. D., Rouse, W. R., Culf, A. D., Spence, C., Boudreau, L. D., Jasper, J. N., ... & Verseghy, D.
523 2000. Eddy covariance measurements of evaporation from Great Slave lake, Northwest Territories,
524 Canada. Water Resources Research, 36(4), 1069−1077.

525 Blanken, P. D., Spence, C., Hedstrom, N., & Lenters, J. D. 2011. Evaporation from Lake Superior: 1.
526 Physical controls and processes. Journal of Great Lakes Research, 37(4), 707–716.

527 Bowen, I. S. 1926. The ratio of heat losses by conduction and by evaporation from any water surface.
528 Physical Review, 27(6), 779.

529 Cai, Y., Ke, C. Q., Li, X., Zhang, G., Duan, Z., & Lee, H. 2019. Variations of lake ice phenology on the
530 Tibetan Plateau from 2001 to 2017 based on MODIS data. Journal of Geophysical Research:
531 Atmospheres, 124(2), 825–843.

532 Christner, E., Kohler, M., & Schneider, M. 2017. The influence of snow sublimation and meltwater
533 evaporation on δD of water vapor in the atmospheric boundary layer of central Europe. Atmospheric
534 Chemistry and Physics, 17(2), 1207–1225.

535 Dalton, J. 1802. Experimental essays on the constitution of mixed gases; on the force of stream or vapor
536 from water and other liquids, both in a Torricellian vacuum and in air; on evaporation; and on the
537 expansion of gases by heat. Proceedings of Manchester Literary and Philosophica Society, 5, 536–602.

538 Deegan, R. D., Bakajin, O., Dupont, T. F., Huber, G., Nagel, S. R., & Witten, T. A. 1997. Capillary flow
539 as the cause of ring stains from dried liquid drops. Nature, 389(6653), 827–829.

540 Deegan, R. D., Bakajin, O., Dupont, T. F., Huber, G., Nagel, S. R., & Witten, T. A. 2000. Contact line
541 deposits in an evaporating drop. Physical review E, 62(1), 756.

542 Desai, S., & Ouarda, T. B. M. J. 2021. Regional hydrological frequency analysis at ungauged sites with
543 random. Journal of Hydrology, 594, 125861.

544 Dong, H., Feng, Z., Yang, Y., Li, P., & You, Z. 2021. Sustainability assessment of critical natural capital:
545 a case study of water resources in Qinghai Province, China. Journal of Cleaner Production, 286, 125532.

546 Falge, E., Baldocchi, D., Olson, R., Anthoni, P., Aubinet, M., Bernhofer, C., ... & Wofsy, S. (2001). Gap
547 filling strategies for defensible annual sums of net ecosystem exchange. Agricultural and forest
548 meteorology, 107(1), 43–69.

549 Finch, J., & Calver, A. 2008. Methods for the quantification of evaporation from lakes. Prepared for the
550 World Meteorological Organization's Commission for Hydrology, 1−41.

551 Froyland, H. K. 2013. Snow loss on the San Francisco peaks: Effects of an elevation gradient on evapo–
552 sublimation (Doctoral dissertation, Northern Arizona University).

553 Froyland, H. K., Untersteiner, N., Town, M. S., & Warren, S. G. 2010. Evaporation from Arctic sea ice
554 in summer during the International Geophysical Year, 1957–1958. Journal of Geophysical Research:
555 Atmospheres, 115, D15104.

556 Gross, M. 2017. The world's vanishing lakes. Current. Biology, 27, 43–46.

557 Guo, Y., Zhang, Y., Ma, N., Song, H., & Gao, H. 2016. Quantifying surface energy fluxes and evaporation
558 over a significant expanding endorheic lake in the central Tibetan Plateau. Journal of the Meteorological
559 Society of Japan. Ser. II, 94, 453–465.

560 Guo, Y., Zhang, Y., Ma, N., Xu, J., & Zhang, T. 2019. Long–term changes in evaporation over Siling Co
561 Lake on the Tibetan Plateau and its impact on recent rapid lake expansion. Atmospheric research, 216,
562 141–150.

563 Hamdani, I., Assouline, S., Tanny, J., Lensky, I. M., Gertman, I., Mor, Z., & Lensky, N. G. 2018. Seasonal
564 and diurnal evaporation from a deep hypersaline lake: The Dead Sea as a case study. Journal of Hydrology,
565 562, 155–167.

566 Han, W. X., Huang, C. L., Gu, J., Hou, J. L., & Zhang, Y. 2021. Spatial–Temporal Distribution of the
567 Freeze–Thaw Cycle of the Largest Lake (Qinghai Lake) in China Based on Machine Learning and
568 MODIS from 2000 to 2020. Remote Sensing, 13(9), 1695.

569 Harbeck, G. E. 1958. Water–loss investigations: Lake Mead studies (Vol. 298). US Government Printing
570 Office.

571 Herrero, J., & Polo, M. J. 2016. Evaposublimation from the snow in the Mediterranean mountains of
572 Sierra Nevada (Spain). The Cryosphere, 10(6), 2981–2998.

573 Huang, L., Liu, J., Shao, Q., & Liu, R. 2011. Changing inland lakes responding to climate warming in
574 Northeastern Tibetan Plateau. Climatic Change, 109(3), 479–502.

575 Huang, W., Li, R., Han, H., Niu, F., Wu, Q., & Wang, W. 2016. Ice processes and surface ablation in a
576 shallow thermokarst lake in the central Qinghai–Tibetan Plateau. Annals of Glaciology, 57(71), 20–28.

577 Jambon–Puillet, E., Shahidzadeh, N., & Bonn, D. 2018. Singular sublimation of ice and snow crystals.
578 Nature communications, 9(1), 1–6.

579 Jin, Z. D., An, Z. S., Yu, J. M., Li, F. C., & Zhang, F. 2015. Lake Qinghai sediment geochemistry linked
580 to hydroclimate variability since the last glacial. Quaternary Science Reviews, 122(2015), 63–73.

581 Kuang, X., and Jiao, J. J. 2016, Review on climate change on the Tibetan Plateau during the last half

582   century, Journal of Geophysical Research, 121, 3979–4007.

583   Lee C.H. 1927. Discussion of "Evaporation on reclamation projects" by IE Houk. Transactions of the
584   American Society of Civil Engineers, 90, 340−343.

585   Lensky, N. G., Lensky, I. M., Peretz, A., Gertman, I., Tanny, J., & Assouline, S. 2018. Diurnal Course of
586   evaporation from the dead sea in summer: A distinct double peak induced by solar radiation and night
587   sea breeze. Water Resources Research, 54(1), 150–160.

588   Li, B., Zhang, J., Yu, Z., Liang, Z., Chen, L., & Acharya, K. 2017. Climate change driven water budget
589   dynamics of a Tibetan inland lake. Global and Planetary Change, 150, 70–80.

590   Li, X. Y., Ma, Y. J., Huang, Y. M., Hu, X., Wu, X. C., Wang, P., ... & Liu, L. 2016. Evaporation and
591   surface energy budget over the largest high-altitude saline lake on the Qinghai-Tibet Plateau. Journal of
592   Geophysical Research: Atmospheres, 121(18), 10–470.

593   Li, X. Y., Shi, F. Z., Ma, Y. J., Zhao, S. J., & Wei, J. Q. 2022. Significant winter CO_2 uptake by saline
594   lakes on the Qinghai–Tibet Plateau. Global Change Biology, 2022, 28(6), 2041–2052.

595   Li, Z., Lyu, S., Ao, Y., Wen, L., Zhao, L., & Wang, S. 2015. Long−term energy flux and radiation balance
596   observations over lake Ngoring, Tibetan Plateau. Atmospheric Research, 155, 13−25.

597   Lin, Y., Cai, T., & Ju, C. 2020. Snow evaporation characteristics related to melting period in a forested
598   permafrost region. Environmental Engineering & Management Journal (EEMJ), 19(3).

599   Liu, C., Zhu, L., Wang, J., Ju, J., Ma, Q., Qiao, B., ... & Kai, J. 2021. In–situ water quality investigation
600   of the lakes on the Tibetan Plateau. Science Bulletin. 66(17). 1727–1730.

601   Liu, H., Feng, J., Sun, J., Wang, L., & Xu, A. 2015. Eddy covariance measurements of water vapor and
602   CO 2 fluxes above the Erhai Lake. Science China Earth Sciences, 58(3), 317–328.

603   Ma, N., Szilagyi, J., Niu, G. Y., Zhang, Y., Zhang, T., Wang, B., & Wu, Y. 2016. Evaporation variability
604   of Nam Co Lake in the Tibetan Plateau and its role in recent rapid lake expansion. Journal of Hydrology,
605   537, 27–35.

606   Messager, M. L., Lehner, B., Grill, G., Nedeva, I., & Schmitt, O. 2016. Estimating the volume and age
607   of water stored in global lakes using a geo–statistical approach. Nature communications, 7(1), 1–11.

608   Mohammed, I. N., & Tarboton, D. G. 2012. An examination of the sensitivity of the Great Salt Lake to
609   changes in inputs. Water Resources Research, 48(11), W11511.

610   Mor, Z., Assouline, S., Tanny, J., Lensky, I. M., & Lensky, N. G. 2018. Effect of water surface salinity
611   on evaporation: The case of a diluted buoyant plume over the Dead Sea. Water Resources Research, 54(3),
612   1460–1475.

613   Nelson, J. 1998. Sublimation of ice crystals. Journal of the atmospheric sciences, 55(5), 910–919.

614   Nordbo, A., Launiainen, S., Mammarella, I., Leppäranta, M., Huotari, J., Ojala, A., & Vesala, T. 2011.
615   Long−term energy flux measurements and energy balance over a small boreal lake using eddy covariance
616   technique. Journal of Geophysical Research: Atmospheres, 116, D02119.

617   Obianyo, J. I. 2019. Effect of Salinity on Evaporation and the Water Cycle. EmergingScience Journal,

618   3(4), 256–262.

619   Persson, P. O. G., Fairall, C. W., Andreas, E. L., Guest, P. S., & Perovich, D. K. 2002. Measurements

620   near the Atmospheric Surface Flux Group tower at SHEBA: Near-surface conditions and surface energy

621   budget. Journal of Geophysical Research: Oceans, 107(C10), SHE–21.

622   Penman, H. L. 1948. Natural evaporation from open water, bare soil and grass. Proceedings of the Royal

623   Society of London. Series A. Mathematical and Physical Sciences, 193(1032), 120−145.

624   Pour, H. K., Duguay, C. R., Scott, K. A., & Kang, K. K. 2017. Improvement of lake ice thickness retrieval

625   from MODIS satellite data using a thermodynamic model. IEEE Transactions on Geoscience and Remote

626   Sensing, 55(10), 5956-5965.

627   Qiu, Y., Xie, P., Leppäranta, M., Wang, X., Lemmetyinen, J., Lin, H., & Shi, L. 2019. MODIS–based

628   daily lake ice extent and coverage dataset for Tibetan Plateau. Big Earth Data, 3(2), 170–185.

629   Roderick M.L. & Farquhar, G.D. 2022. The cause of decreased pan evaporation over the past 50 years.

630   Science 298, 1410-1411.

631   Salhotra, A. M., Adams, E. E., & Harleman, D. R. 1985. Effect of Salinity and Ionic Composition on

632   Evaporation: Analysis of Dead Sea Evaporation Pans. Water Resources Research, 21(9), 1336–1344.

633   Salhotra, A. M., Adams, E. E., & Harleman, D. R. 1987. The alpha, beta, gamma of evaporation from

634   saline water bodies. Water Resources Research, 23(9), 1769–1774.

635   Sow, A., Traore, I., Diallo, T., Traore, M., & Ba, A. 2022. Comparison of Gaussian process regression,

636   partial least squares, random forest and support vector machines for a near infrared calibration of

637   paracetamol samples. Results in Chemistry, 4, 100508.

638   Stepanenko, V. M., Repina, I. A., Ganbat, G., & Davaa, G. 2019. Numerical simulation of ice cover of

639   saline lakes. Izvestiya, Atmospheric and Oceanic Physics, 55, 129-138.

640   Su, D. S., Hu, X. Q., Wen, L. J., Lyu, S. H., Gao, X. Q., Zhao, L., … & Kirillin, G. 2019. Numerical

641   study on the response of the largest lake in China to climate change. Hydrology and Earth System

642   Sciences, 23, 2093–2109.

643   Tang, L. Y., Duan, X. F., Kong, F. J., Zhang, F., Zheng, Y. F., Li, Z., … & Hu, S. J. 2018. Influences of

644   climate change on area variation of Qinghai Lake on Qinghai–Tibetan Plateau since 1980s. Scientific

645   Report, 8, 7331–7338.

646   Tian, W., Liu, X., Wang, K., Bai, P., & Liu, C. 2021. Estimation of reservoir evaporation losses for China.

647   Journal of Hydrology, 596, 126142.

648   Vercauteren, N., Bou–Zeid, E., Huwald, H., Parlange, M. B., & Brutsaert, W. 2009. Estimation of wet

649   surface evaporation from sensible heat flux measurements. Water Resources Research, 45(6), W06424.

650   Wan, W., Zhao, L., Xie, H., Liu, B., Li, H., Cui, Y., ... & Hong, Y. 2018. Lake surface water temperature

651   change over the Tibetan plateau from 2001 to 2015: A sensitive indicator of the warming climate.

652   Geophysical Research Letters, 45(20), 11–177.

653   Wang, B., Ma, Y., Chen, X., Ma, W., Su, Z., & Menenti, M. 2015. Observation and simulation of lake-

air heat and water transfer processes in a high-altitude shallow lake on the Tibetan Plateau. Journal of Geophysical Research: Atmospheres, 120(24), 12327–12344.

Wang, B., Ma, Y., Wang, Y., Su, Z., & Ma, W. 2019a. Significant differences exist in lake–atmosphere interactions and the evaporation rates of high–elevation small and large lakes. Journal of hydrology, 573, 220–234.

Wang, B., Ma, Y., Ma, W., Su, B., & Dong, X. 2019b. Evaluation of ten methods for estimating evaporation in a small high–elevation lake on the Tibetan Plateau. Theoretical and applied climatology, 136(3), 1033–1045.

Wang, B., Ma, Y., Su, Z., Wang, Y., & Ma, W. 2020. Quantifying the evaporation amounts of 75 high–elevation large dimictic lakes on the Tibetan Plateau. Science advances, 6(26), eaay8558.

Wang, W., Lee, X., Xiao, W., Liu, S., Schultz, N., Wang, Y., ... & Zhao, L. 2018. Global lake evaporation accelerated by changes in surface energy allocation in a warmer climate. Nature Geoscience, 11(6), 410–414.

Wang, W., Xiao, W., Cao, C., Gao, Z., Hu, Z., Liu, S., ... & Lee, X. 2014. Temporal and spatial variations in radiation and energy balance across a large freshwater lake in China. Journal of Hydrology, 511, 811−824.

Woolway, R. I., Kraemer, B. M., Lenters, J. D., Merchant, C. J., O'Reilly, C. M., & Sharma, S. 2020. Global lake responses to climate change. Nature Reviews Earth & Environment, 1(8), 388–403.

Woolway, R. I., Verburg, P., Lenters, J. D., Merchant, C. J., Hamilton, D. P., Brookes, J., ... & Jones, I. D. 2018. Geographic and temporal variations in turbulent heat loss from lakes: A global analysis across 45 lakes. Limnology and Oceanography, 63(6), 2436–2449.

Wu, H., Huang, Q., Fu, C., Song, F., Liu, J., & Li, J. 2021. Stable isotope signatures of river and lake water from Poyang Lake, China: Implications for river–lake interactions. Journal of Hydrology, 592, 125619.

Wu, H., Song, F., Li, J., Zhou, Y., Zhang, J., & Fu, C. 2022. Surface water isoscapes ($\delta18O$ and $\delta2H$) reveal dual effects of damming and drought on the Yangtze River water cycles. Journal of Hydrology, 610, 127847.

Wurtsbaugh, W. A., Miller, C., Null, S. E., DeRose, R. J., Wilcock, P., Hahnenberger, M., ... & Moore, J. 2017. Decline of the world's saline lakes. Nature Geoscience, 10(11), 816–821.

Xiao, M., & Cui, Y. 2021. Source of evaporation for the seasonal precipitation in the Pearl River Delta, China. Water Resources Research, e2020WR028564.

Xie, F., Lu, P., Leppäranta, M., Cheng, B., Li, Z., Zhang, Y., ... & Zhou, J. 2023. Heat budget of lake ice during a complete seasonal cycle in lake Hanzhang, northeast China. Journal of Hydrology, 620, 129461.

Yang, K., Hou, J., Wang, J., Lei, Y., Zhu, L., Chen, Y., ... & He, X. 2021. A new finding on the prevalence of rapid water warming during lake ice melting on the Tibetan Plateau. Science Bulletin, 66(23), 2358–2361.

Yang, K., Wu, H., Qin, J., Lin, C., Tang, W., & Chen, Y. 2014. Recent climate changes over the Tibetan

691 Plateau and their impacts on energy and water cycle: A review. Global and Planetary Change, 112, 79–
692 91.

693 Zhang, Q., & Liu, H. 2014. Seasonal changes in physical processes controlling evaporation over inland
694 water. Journal of Geophysical Research: Atmospheres, 119(16), 9779–979.

695 Zhu, L., Yang, K., Wang, J., Lei, Y., Chen, Y., Zhu, L., ... & Qin, J. 2016. Quantifying evaporation and
696 its decadal change for Lake Nam Co, central Tibetan Plateau. Journal of Geophysical Research:
697 Atmospheres, 121(13), 7578–7591.

Figure Legends

699 **Figure 1. Location of Qinghai Lake (below) and the measurement site of the Chinese Torpedo**

700 **Qinghai Lake test base (upper).** The insets in the upper picture are photos of the four–way radiometer

701 and infrared thermometer (left), meteorological variable measurements (middle), and eddy covariance

702 sensors (right). The scale is just for the Qinghai Lake Basin.

703 **Figure 2. Diurnal characteristics of evaporation (E), latent heat flux (LE), sensible heat flux (H),**

704 **heat storage change (G), and net radiation (Rn) of Qinghai Lake (QHL) during the ice–free and**

705 **ice–covered periods (IFP and ICP) from 2014 to 2018.** The multiday average 30–min data during the

706 IFP and ICP in each cycle year are shown here, and the colored shading indicates a 0.5 standard deviation.

707 The gray area indicates nighttime. The labels 2014/2015, 2015/2016, 2016/2017, 2017/2018, and

708 2018/2019 indicate the cycle year of the freeze–thaw cycles.

709 **Figure 3. Evaporation (E) rate (a, c, and e) and annual E sum (b, d, and f) of Qinghai Lake (QHL)**

710 **during the cycle year (annual: AN), ice–free and ice–covered periods (IFP and ICP) in each cycle**

711 **year from 2014 to 2018.** a and b show daily data, c and d show daytime data, and e and f show nighttime

712 data. The whiskers in a, c, and e show the 1.5 interquartile range, while the letter associated with the

713 whiskers indicates statistically significant differences via one–way ANOVA during the different freeze–

714 thaw periods in each year from 2014 to 2018. The labels 2014/2015, 2015/2016, 2016/2017, 2017/2018,

715 and 2018/2019 indicate the cycle year of freeze–thaw cycling.

716 **Figure 4. Sensitivity coefficient between the daytime and nighttime climatic factors and**

717 **evaporation (E) rate of Qinghai Lake (QHL) during the ice–free and ice–covered periods (IFP and**

718 **ICP).** *, **, and *** indicate statistical significance at the $P < 0.1$, $P < 0.05$, and $P < 0.01$ levels,

719 respectively, via Student's t tests. Rn, Δe. WS, WD, Pres, Ta−Ts, Tl, and ICR indicate the net radiation,

720 vapor pressure difference, wind speed, wind direction, Pres, difference between the air and lake surface

721 temperatures, average temperature of the lake body from 0 to 300 cm, and ice coverage rate, respectively.

722 **Figure 5. Interannual variability in the simulated evaporation (E) rate (a~c) and annual E sum**

723 **(d~f) of Qinghai Lake (QHL) in the cycle year (annual: AN), ice–free and ice–covered periods (IFP**

724 **and ICP) from 2003 to 2017.** The blue shading indicates a 0.5 standard deviation, and the red shading
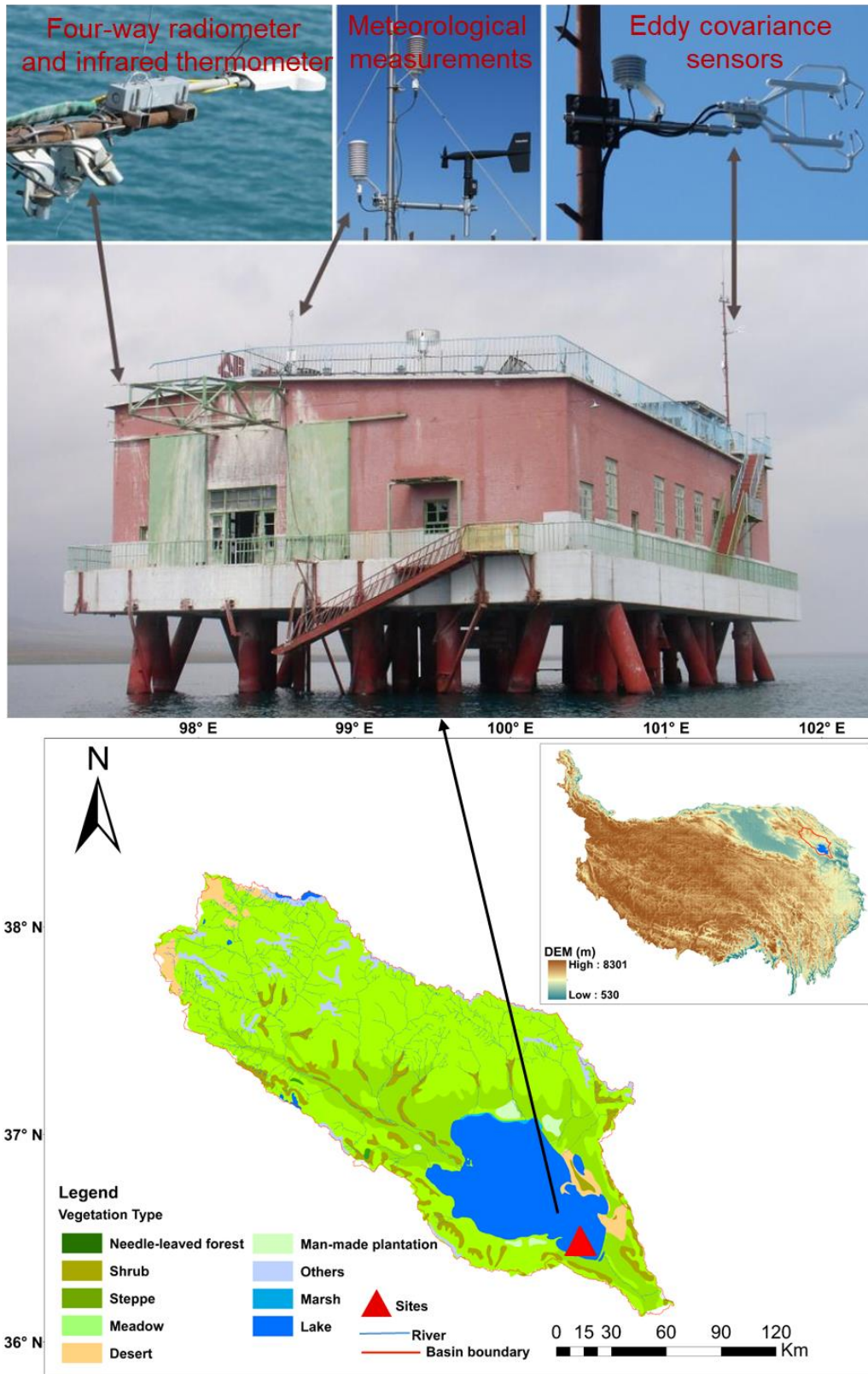
725   indicates the 95% confidence interval of the trend line.

726   **Figure 6. Evaporation (E) and heat storage change (G) in Qinghai Lake (QHL) during the ice–free**

727   **and ice–covered periods (IFP and ICP).** WS, Pres, Δe, Ta−Ts, Rn, and ICR are the wind speed, air

728   pressure, vapor pressure difference, difference between Ta and Ts, net radiation, and ice coverage rate of

729   the lake, respectively. The red plus sign indicates a positive effect of the variable on E.

730   **Figure 7. The multiyear average contribution of the changes in air temperature (Ta), lake surface**

731   **temperature (Ts), downward shortwave radiation (Rs), and wind speed (WS) to the simulated**

732   **evaporation (E) of Qinghai Lake (QHL) in the cycle year (annual: AN), ice–free and ice–covered**

733   **periods (IFP and ICP) from 2003 to 2017**. a shows the multiyear average change in the E rate caused

734   by Ta, Ts, Rs, and WS; b shows the multiyear average change in the annual E sum caused by Ta, Ts, Rs,

735   and WS; and c shows the multiyear average change percentage of E caused by Ta, Ts, Rs, and WS. The
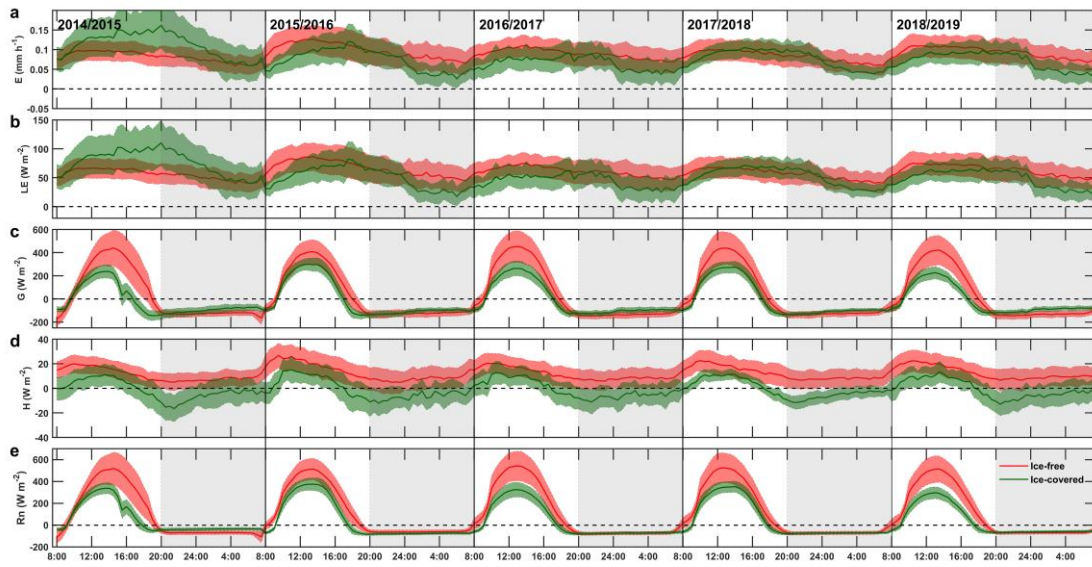
736   whiskers indicate a 0.5 standard deviation.
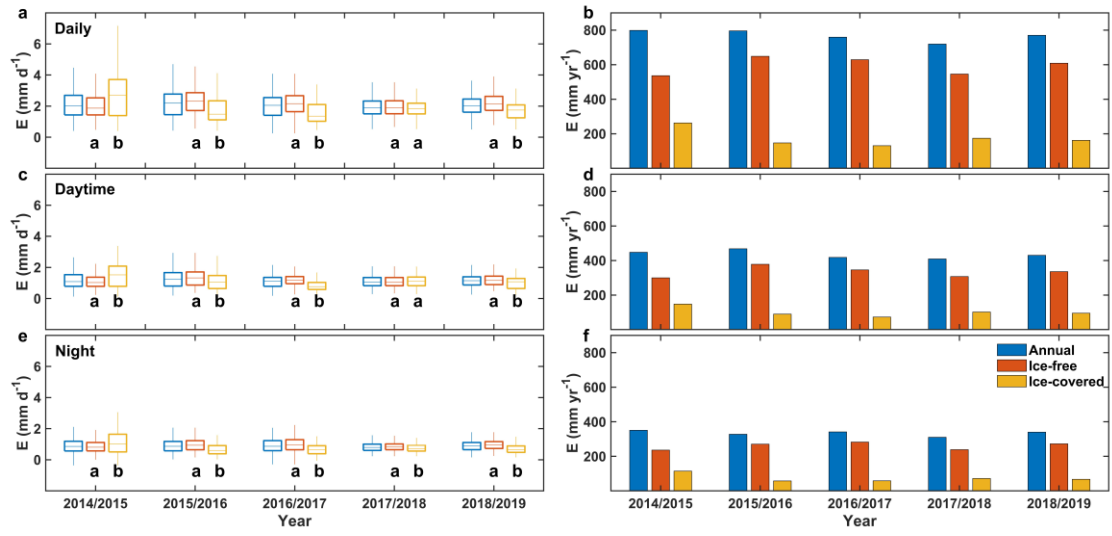
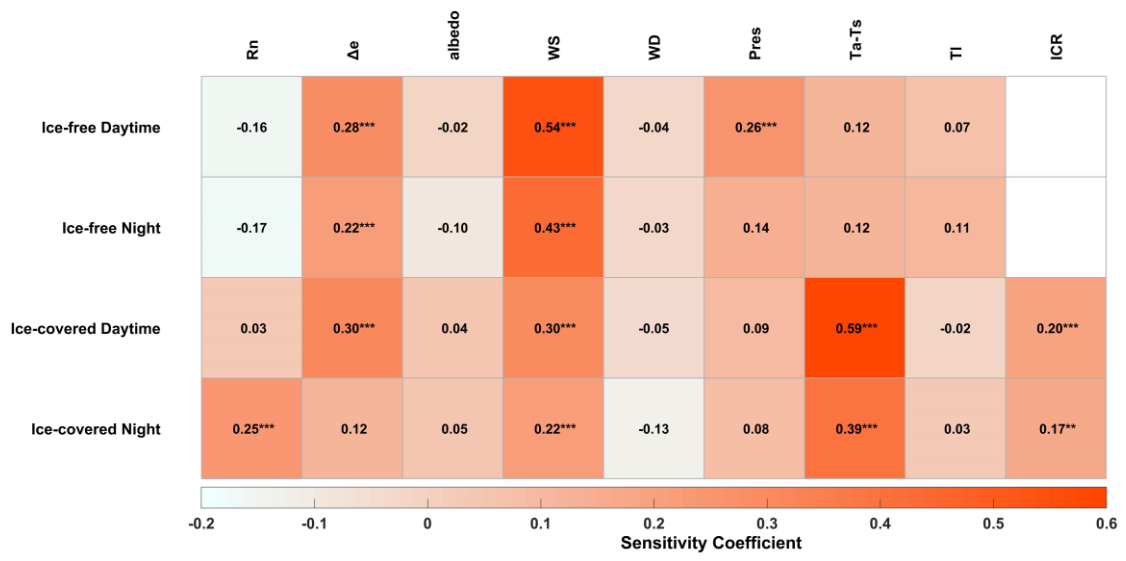737 **Figures**

738 **Figure 1.**

739

Figure 2.

744   **Figure 3.**

745

746

	Rn	Δe	albedo	WS	WD	Pres	Ta-Ts	TI	ICR
Ice-free Daytime	-0.16	0.28***	-0.02	0.54***	-0.04	0.26***	0.12	0.07	
Ice-free Night	-0.17	0.22***	-0.10	0.43***	-0.03	0.14	0.12	0.11	
Ice-covered Daytime	0.03	0.30***	0.04	0.30***	-0.05	0.09	0.59***	-0.02	0.20***
Ice-covered Night	0.25***	0.12	0.05	0.22***	-0.13	0.08	0.39***	0.03	0.17**

-0.2   -0.1   0   0.1   0.2   0.3   0.4   0.5   0.6
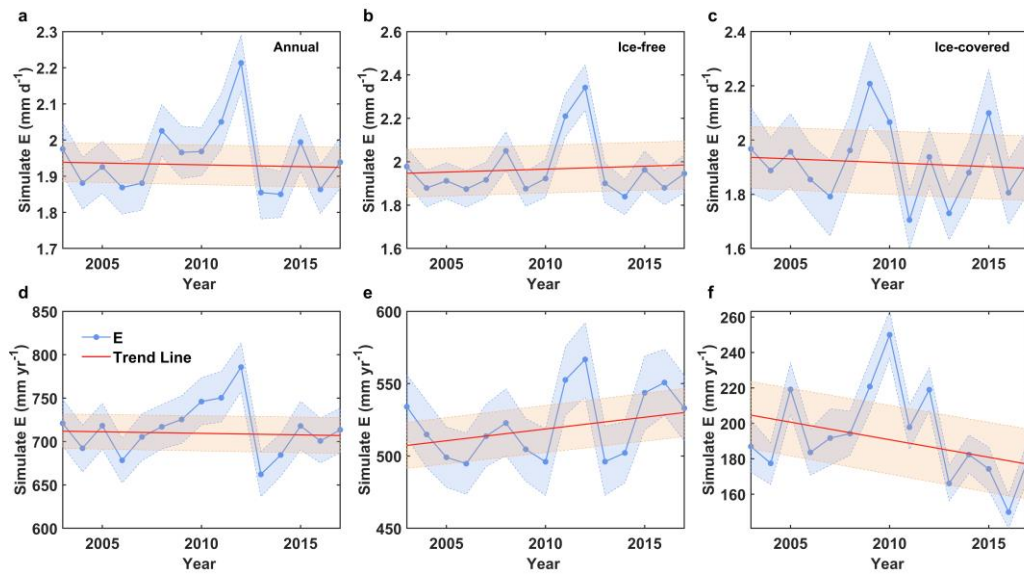
Sensitivity Coefficient

748

749
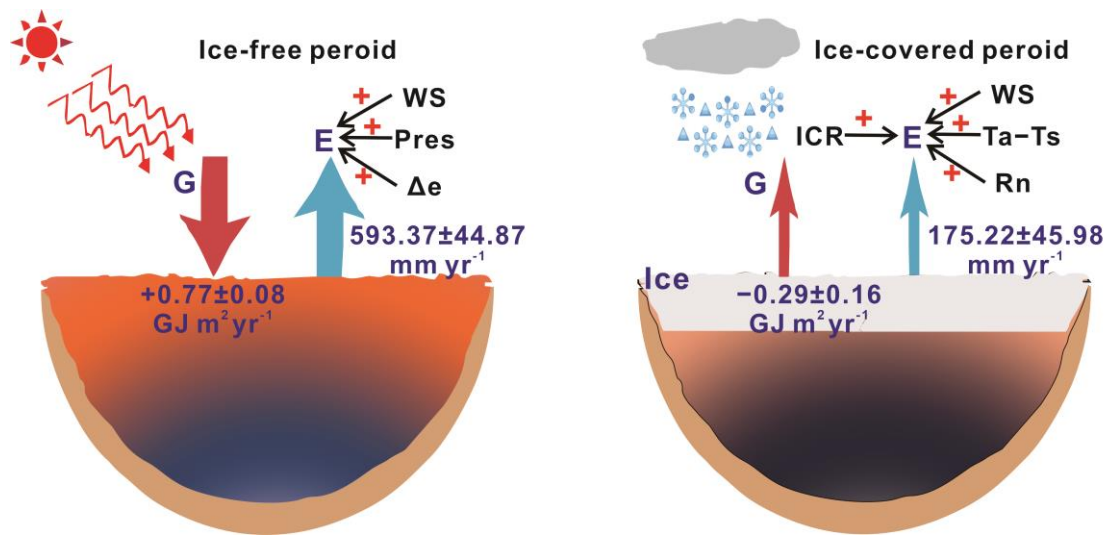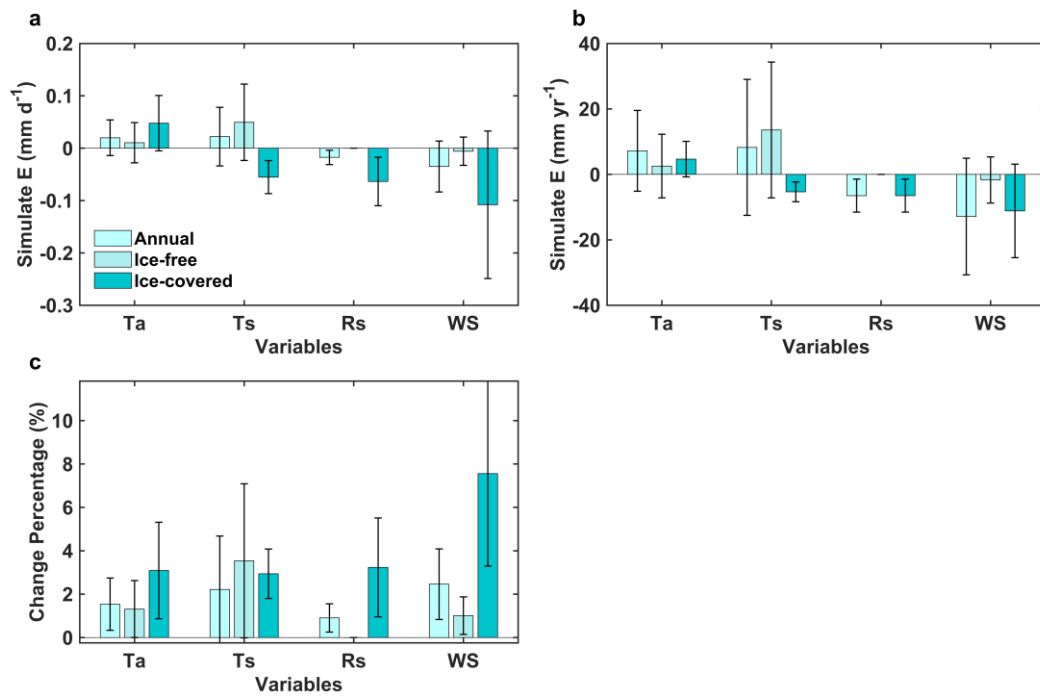
750 **Figure 5.**

751

752

753 **Figure 6.**

754

755

756   **Figure 7.**